MAGRAC--RAILGUN SIMULATION PROGRAM

F. J. Deadrick
R. S. Hawke
J. K. Scudder

March 25, 1981
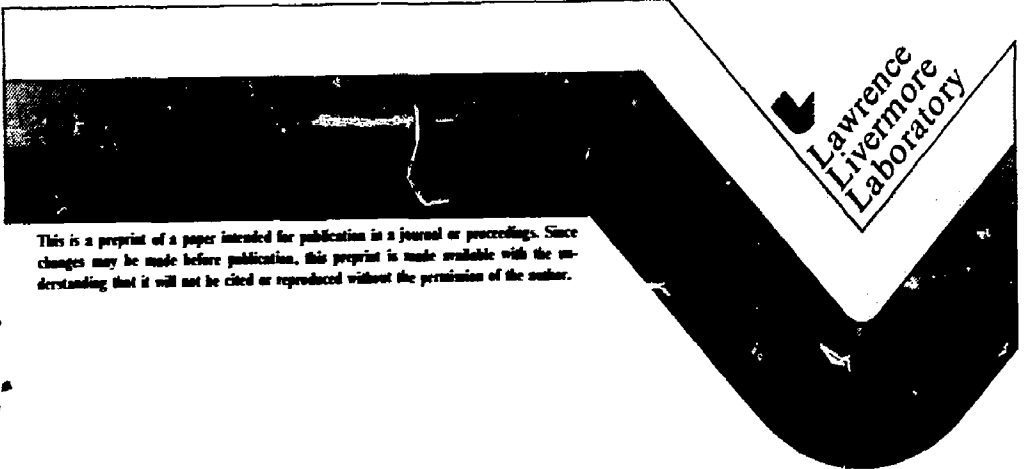
Lawrence
Livermore
Laboratory

P. J. Deadrick[†], R. S. Hawke[†] and J. D. Scudder[**]

Abstract - We have developed and validated a
computer simulation code at the Lawrence Livermore
National Laboratory (LLNL) to predict the performance
of a railgun electromagnetic accelerator. The code,
called MAGRAC (MAGnetic Railgun ACcelerator), models
the performance of a railgun driven by a magnetic flux
compression current generator (MFCG). The MAGRAC code
employs a time-step solution of the nonlinear
time-varying element railgun circuit to determine rail
currents. From the rail currents, the projectile
acceleration, velocity, and position are found. We
have validated the MAGRAC code through a series of
eight railgun tests conducted jointly with the Los
Alamos National Laboratory. This paper describes the
formulation of the MAGRAC railgun model and compares
the predicted current waveforms with those obtained
from full-scale experiments.

INTRODUCTION

MAGRAC (MAGnetic Railgun ACcelerator) is a
computer code designed to model an electromagnetic
railgun projectile launcher and power source. The
MAGRAC code uses both electrical and mechanical
parameters of the railgun, projectile, and primary
energy source to compute the resulting currents and
accelerating forces on the projectile as a function of
time. The code employs an implicit finite-difference
solution technique which allows the inclusion of
time-varying nonlinear elements in the railgun model.

In this paper we describe the model elements used
in the MAGRAC code and compare some computed results
with railgun test data. Three series of tests have
been conducted in collaboration with the Los Alamos
National Laboratory to test the performance of railgun
accelerators. These tests included both 0.9-m and
1.8-m long railguns with square bores of 12.7 mm that
were used to launch 3.1-g polycarbonate projectiles.
Also a short, 0.3-m long, 50-mm square bore gun was
used to launch a 165-gram projectile. In each of
these tests, a magnetic flux compression generator [1]
(MFCG) was used as the primary energy source to power
the railgun. The MAGRAC model includes both the
railgun and a variety of power sources including the
MFCG.

We first provide brief details of the railgun and
the MFCG. We then describe the computer solution
technique and conclude with representative comparisons
between computer prediction and experiment.

MAGRAC Models

Figure 1 shows a simplified, schematic
illustration of a railgun. A railgun is essentially a
linear dc motor consisting of a pair of rigid parallel
bars (rails) that carry current to and from a small
interconnecting movable conductor. The conducting
link functions as an armature, while the parallel
rails serve as a single-turn field winding. The
Lorentz force resulting from the armature current
interacting with the magnetic field generated by the
rail current accelerates the armature and the
projectile.

While railguns may be driven by a number of
primary energy sources such as capacitor banks and
homopolar generators, we discuss only the MFCG in this
paper.

The MFCG-railgun system used by the joint Los
Alamos/LLNL team is shown in Fig. 2. The capacitor
bank provides the initial energy to the circuit, and
the MFCG extends the duration of the current pulse
delivered to the railgun. When the switch is closed,
the capacitor bank generates a current in the MFCG
which acts as a temporary storage inductor. As the
current approaches near maximum, the explosive is
initiated by a single detonator. The explosive drives
the top conductor of the MFCG into the bottom
conductor, isolates the capacitor bank source at point
A, forms a closed MFCG-railgun circuit, and continues
to progressively implode the MFCG. The resulting
decrease in inductance tends to sustain the current,
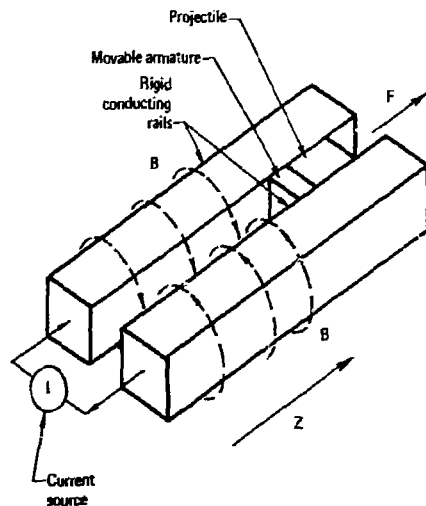while energy is consumed by the railgun and losses.

Fig. 1. Schematic of railgun showing the current
path I, the magnetic flux lines B, and the resultant
force F that drives the projectile. Initially there
is a thin metallic fuse in back of the projectile
that completes the circuit; this vaporizes almost
immediately forming a plasma that continues to carry
current and accelerate the projectile in the
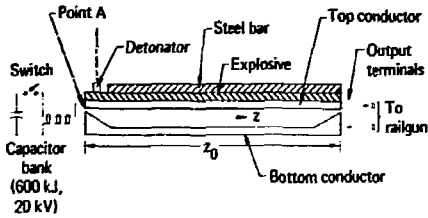direction Z.

1

Fig. 2. Side view of a magnet flux compression generator. When the detonator ignites the high explosive, the top conductor is driven down to short the bottom conductor. The explosive then causes the short to propagate in the z direction, compressing the enclosed flux.

Railgun Model

The railgun portion of the model is basically very simple in form. Two copper rails provide the current path for the accelerator. A small fuse is placed at the breech end of the gun section directly behind the projectile. The fuse serves two purposes, the first being to provide a current path for the initial MFCG current charge, and secondly to generate a plasma arc between the rails to act as a movable conducting armature.

An electrical equivalent circuit of the railgun section is shown in Fig. 3. $R(x,t,I)$ is the rail resistance term which changes as a function of the plasma armature position x, time t, and rail current I. Rail heating occurs as a result of the resistive energy loss which increases the temperature and resistivity of the rails. The effective rail resistivity ρ (see appendix A) is represented by the relation

$$\rho = \rho_0 + \beta\,\frac{I}{p} \quad , \tag{1}$$

where ρ_0 is the initial resistivity of the copper rails, β is a temperature-dependent resistivity coefficient, and p is the width of the rails. Time-dependent diffusion of a constant current into the rails in combination with a freely accelerating projectile leads to an effective rail resistance gradient (effective resistance per unit rail length) R_1 (see appendix B)

$$R_1 = \frac{8}{3p}\,(\pi\mu\rho/2t)^{1/2} \quad , \tag{2}$$

where μ is the permeability of the rail material, and t is the length of time that the current has been flowing.

The inductance L of the rail pair enters into both the electrical circuit equations and the equations of motion. Electrically, as the armature moves down the bore of the railgun, both the gun resistance and inductance increase, as more of the rail pair is included in the circuit. The resulting inductive voltage V_L is given by:

$$V_L = \frac{d(LI)}{dt} = L\frac{dI}{dt} + I\frac{dL}{dt} \quad , \tag{3}$$

where

$$L = L_1 x, \tag{4}$$

$$\frac{dL}{dt} = L_1\frac{dx}{dt} = L_1 v \quad , \tag{5}$$

and L_1 is the inductance gradient (inductance per unit length of the rail pair), and v is the armature velocity.

A third term, the plasma arc voltage drop V_{Arc}, is also included in the model, as shown in Fig. 3.

When the fuse vaporizes and establishes the initial plasma arc, the plasma acts as a movable conductor which "pushes" on the projectile and accelerates the mass down the barrel of the gun. The Lorentz force F_p on the projectile is given by

$$F_p = \frac{L_1 I^2}{2} \quad , \tag{6}$$

and the projectile acceleration a is

$$a = \frac{L_1 I^2}{2m} \quad , \tag{7}$$

where m is the mass of the projectile. Projectile velocity and position are then obtained from the first and second integrals of the projectile acceleration, respectively.

MFCG Model

The model for the flux compression generator is similar in form to that of the railgun model in that the MFCG is primarily a time-varying inductor and resistor. Figure 4 illustrates the electrical equivalent circuit model for the MFCG and the capacitor bank used to supply the initial generator current.

In the initial state, the switch S_2 is open, and S_1 is closed at $t = 0$ to connect the capacitor bank to the compression generator. The RLC elements of the capacitor bank, MFCG, and railgun fuse form a damped resonant circuit which has a sinusoidal current buildup in the MFCG. One typically closes the switch S_2 near the peak current of the first-quarter cycle.

The MAGRAC model includes both the capacitor bank charge-up cycle and the compression of the MFCG which is modeled as a short which moves down the length of the MFCG at the explosive detonation velocity. The MFCG resistance term R_F is modeled as a function of the position of the short, the time, and the current.

The resistance is calculated from the MFCG conductor resistivity ρ_F where

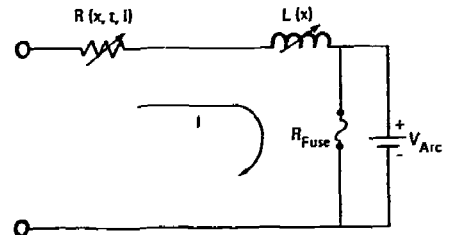$$\rho_F = \rho_{F0} + \beta_F\!\left(\frac{I_F}{p_F}\right) \quad , \tag{8}$$

Fig. 3. Electrical equivalent circuit of railgun. $R(x,t,I)$ and $L(x)$ are the lumped equivalents of the rail resistance and inductance which change as the projectile moves down the railgun. The fuse is first vaporized to initiate the plasma arc and start the projectile acceleration. V_{Arc} is the plasma arc voltage drop (typically 50-300 V).
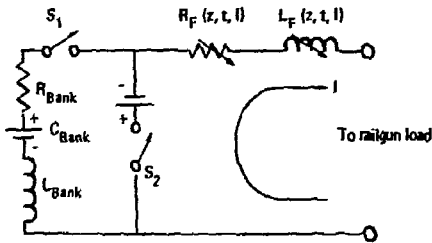
2

Fig. 4. MFCG equivalent circuit. The closure of S_1 initiates the discharge of the capacitor bank into the MFCG-railgun system. The closure of S_2 corresponds to the beginning of the MFCG implosion and R_F and L_F are the lumped equivalents of the MFCG resistance and inductance which decrease with time.

ρ_{F0} is the initial resistivity of the MFCG conductors and β_F is a temperature-dependent resistivity coefficient (see Appendix A). I_F is the MFCG current and p_F is the width of the flux compression conductors. The effective resistance gradient R_{1F} of the MFCG (see appendix B) is then evaluated as a function of time and current,

$$R_{1F} = \frac{1}{p_F} (\pi \mu \rho_F / 2t)^{1/2} . \qquad (9)$$

The equivalent MFCG resistance term for both conductors in the equivalent circuit is

$$R_F = 2R_{1F}(z_0 - z) , \qquad (10)$$

where z_0 is the initial length of the generator and z is the length of MFCG which has been imploded.

The terms for the MFCG inductance are somewhat more complex. As the HE burns, the overall length of the MFCG circuit diminishes and thereby the resistance and inductance in the circuit become smaller. The high currents, on the other hand, force the generator conductors apart. The Los Alamos design uses a steel bar to inertially confine the generator during operation; however, at high current levels the rails of the MFCG move apart resulting in an increase in the inductance. Appendix C describes the technique used to calculate the time-varying inductance gradient L_{1F} from which the MFCG inductance L_F is calculated, where

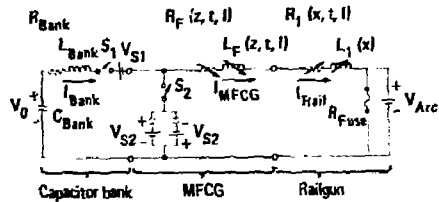$$L_F = L_{1F}(z_0 - z) . \qquad (11)$$

Fig. 5. Complete equivalent circuit of MFCG-powered railgun.

COMPUTER SOLUTION

When the railgun section and the MFCG section are combined as shown in Fig. 5, circuit equations can be written for the various portions of circuit operation, i.e., after S_1 is closed and before S_2 is closed, etc. The capacitor bank charge voltage is used as an initial condition for the start of the simulation. When S_1 is closed, the bank is connected to the MFCG and the railgun fuse shunt. The model integrates the energy dissipated in the fuse to determine the time of vaporization. We evaluate the current by using Kirchoff's law to calculate the derivative of the current circulating in each electrical loop and then incrementally change the current with each iteration. Once each iteration of I(t) is found, we then use this value to compute a new set of values for dI/dt, etc. The MAGRAC code keeps account of the various regions of operation to select the proper expressions for the computation of the circuit currents.

As the MAGRAC code computes the MFCG and railgun currents at each time step, the railgun current is used to calculate the Lorentz accelerating force on the projectile. The projectile acceleration is integrated once to compute the projectile velocity and twice to determine the projectile position. The updated current, velocity, and position values in turn feed back into the evaluation of parameters used to compute the new value of dI/dt.

To illustrate the results obtained from the MAGRAC code, representative computations and experimental measurements are shown in the next section.

NUMERICAL RESULTS

The MAGRAC code has been used to model several of the joint LLNL/Los Alamos railgun experiments conducted at Los Alamos, and has also been used to model the Australian National University homopolar generator-inductor railgun system [2,3]. Table 1

Table 1. Summary of results for the LLNL/Los Alamos Railgun Experiments [4].

	Experiment							
	1A	1C	2A	2B	2C	2D	2E	50-1
Accelerator length (m)	0.9	0.9	1.8	1.8	1.8	1.8	1.8	.27
Accelerator bore (mm)	12.5	12.7	12.7	12.7	12.7	12.7	12.7	50
Projectile mass (g)	2.9	3.1	3.1	3.1	3.1	3.1	3.1	165
Bank capacitance (mF)	1.5	1.5	3.0	3.0	3.0	3.0	3.0	3.0
Charge voltage (kV)	9.5	16.2	11.5	16.1	16.2	16.1	16.1	16.0
Initial energy (kJ)	68	197	198	389	394	389	389	384
Initial current (kA)	285	~458	440	~640	640	625	625	630
Peak current (kA)	575	~860	~860	~970	965	1290	~1250	1950
Launch velocity (km/s)	2.8	5.6	5.4	~9.9	~9.9	~10.1	~10.1	0.35

3

summarizes these experiments. The diagnostics used in these tests included pulsed x rays to observe the projectile in flight; Rogowski coils to monitor the railgun-MFCG current; optical and inductive pickup probes to detect the plasma arc passage along the barrel of the railgun; and foil switches to detect the arrival times of the projectile. These diagnoscics provided measured benchmarks with which to evaluate the numerical MAGRAC model for several different railgun conditions.

75-kJ Short-Circuit Experiment

Shown first in Fig. 6 is the computed and measured current generated by a MFCG into a low-inductance short circuit. Using appropriate initial conditions and an inductance gradient for the MFCG of 0.46 μH/m, we found that the model provided good agreement with the experiment. (The inductance gradient was chosen for best agreement with the experiment.)

70-kJ/12.7-mm-Bore Railgun Experiment

Figures 7(a) through 7(c) show the computed results for a railgun connected to the MFCG. This case, which corresponds to experiment 1A, is for a low-energy (70-kJ)/low-velocity (2.8-km/s) launch. In this experiment, we again obtained good agreement between computed and measured current and the pulsed x-ray shadowgraph of the projectile in flight provided a benchmark for determining model accuracy as shown in Fig. 7(c).

385-kJ/50-mm-Bore Railgun Experiment

Good confirmation of the model has also been obtained for the large-bore 50-mm shot in which a 165-g projectile was launched from a 0.3-m long railgun. Figures 8(a), (b), and (c) show the measured and modeled current pulse, the predicted projectile position vs time, and the velocity vs position. Again, the computed and measured current record matched, and the shadowgraph record corresponded reasonably closely with the calculated position vs time. The slight shadowgraph-position mismatch results from a slightly higher computed velocity[Fig. 8(c)] accentuated by the long free-flight time.

395-kJ/12.7-mm-Bore Railgun Experiment

As a final example, we include a comparison of the measured and modeled results for one of the high-energy (390 kJ)/high-velocity launches. Figures 9(a), (b), and (c) show the measured and modeled current pulse, the predicted projectile position vs time, and the velocity vs position for experiment 2C. Although a good match for the measured and calculated current vs time was obtained, particular sensitivity was observed in the terms containing the rail and flux generator widths, which enter into the calculations for the resistive terms. As discussed in a companion paper[4], shadowgraphs of the projectile after launch were not obtained in the high-energy/small-bore experiments; hence, the position-vs-time calculation cannot be verified as for the above experiments.
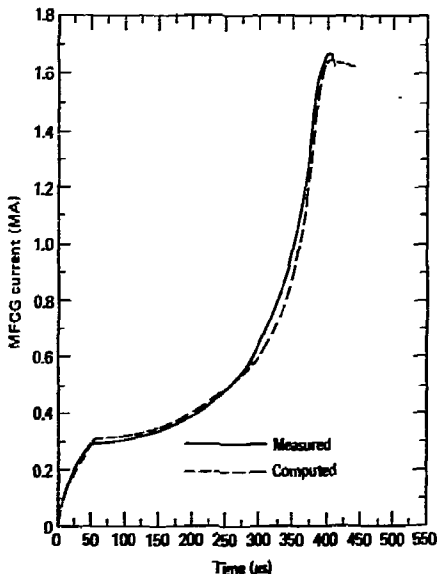

Fig. 6. Computed and measured magnetic flux compression generator current into a low-inductance short circuit shown as a function of time. The 1.5 mf capacitor bank was initially charged to 10 kV.
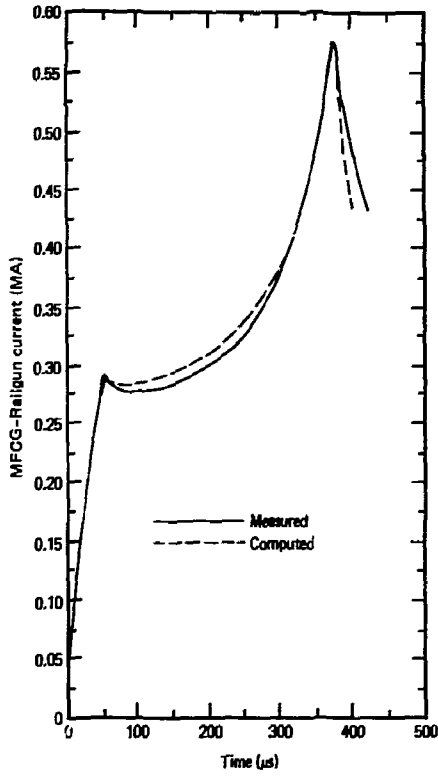
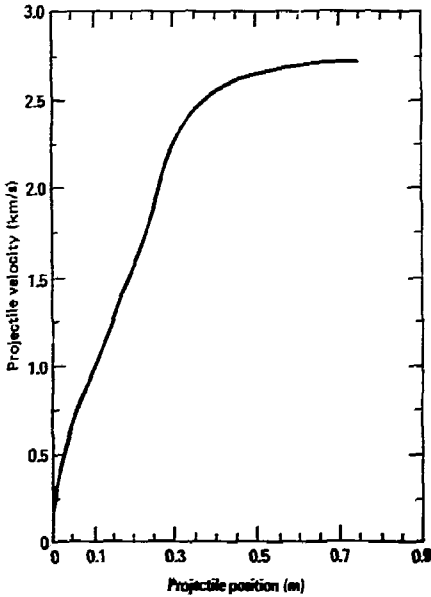Fig. 7(a). Computed and measured current for experiment 1A.

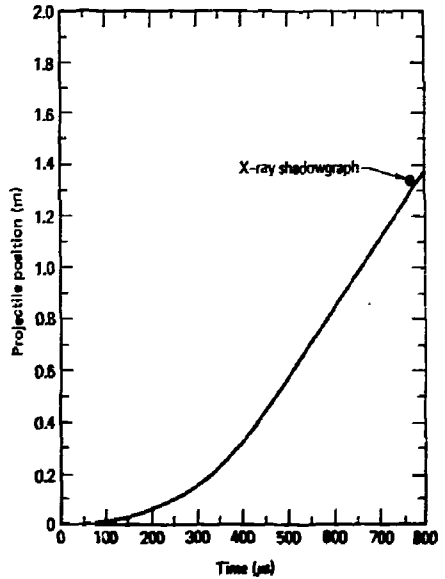Fig. 7(b). Computed projectile velocity for experiment 1A.

Fig. 7(c). Computed projectile position as a function of time for experiment 1A.
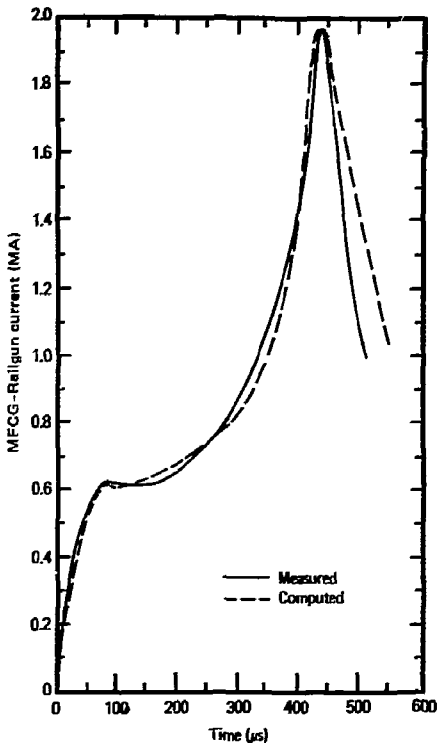
5

Fig. 8(a). Computed and measured current pulse into
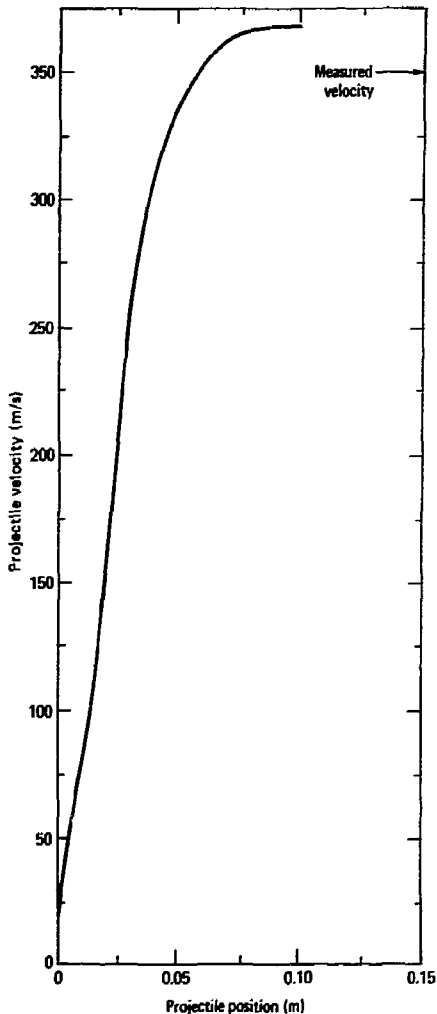50-mm-bore railgun vs time for experiment 50-1.

Fig. 8(c). Computed projectile velocity vs
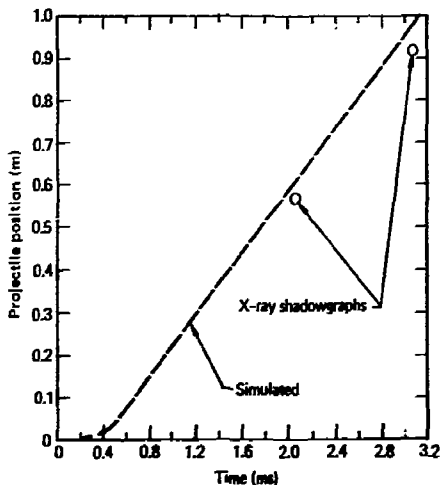projectile position for experiment 50-1.

Fig. 8(b). Computed projectile position as a
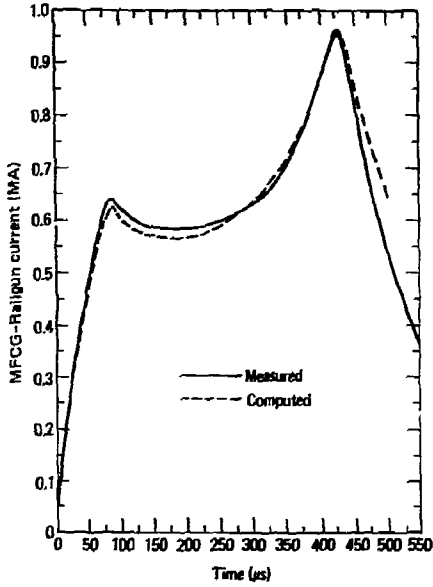function of time for 50-mm-bore railgun with 165-g
projectile.

6

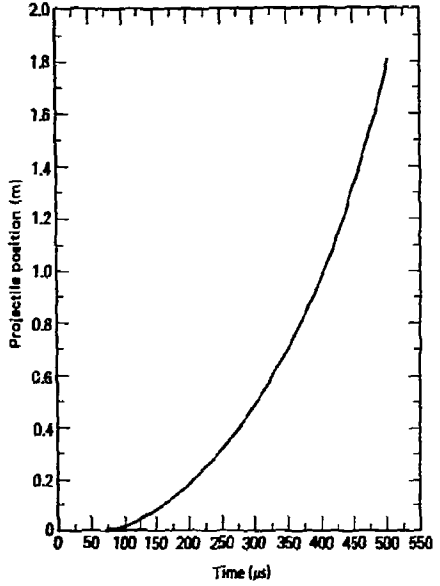Fig. 9(a). Computed and measured current for experiment 2C.

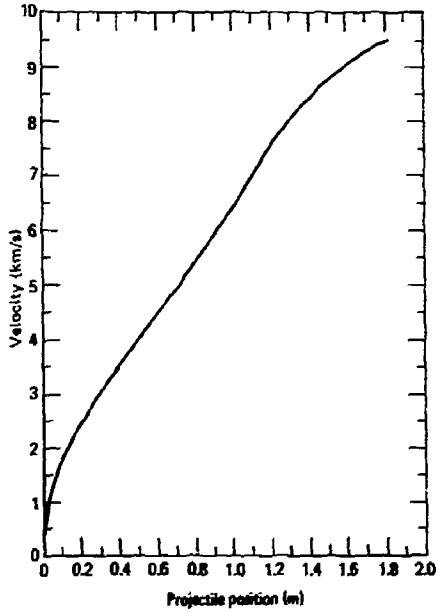Fig. 9(b). Computed projectile position as a function of time for experiment 2C.

Fig. 9(c). Computed projectile velocity vs projectile position for experiment 2C.

CONCLUSIONS

The MAGRAC model has provided valuable insight and data which have directly benefited the design, operation, and diagnostics of MFCG-railgun systems used in the joint Los Alamos/LLNL research project. The agreement between experiment and calculation that was found for a wide variety of experiments has established the usefulness of the MAGRAC model. Further development of the MAGRAC code and the performance of additional experiments will lead to an even firmer foundation for future predictions of railgun performance and potential.

ACKNOWLEDGMENTS

The authors wish to express thanks to those contributing to the development of the MAGRAC railgun model. We offer particular thanks to G. D. Dorough, Jr. and J. W. Kury (LLNL) for their programmatic support, to C. M. Fowler and D. R. Peterson of Los Alamos for their insight and experimental collaboration, and to R. Bevensee of LLNL for assistance in the development of the MFCG model. The help of B. E. Dubois in preparing this paper is gratefully acknowledged.

APPENDIX A. EQUIVALENT RESISTIVITY AS A FUNCTION OF CURRENT CONCENTRATION

The effect of a temperature-dependent resistivity was determined in three steps. First, we simultaneously solved the magnetic diffusion and heat transfer equations to determine the time-dependent current and temperature distributions in a semi-infinite conductor divided into small zones. Second, we used the currents and resistances of the zones to calculate the energy dissipated and the effective resistance as a function of time. Third, we calculated the equivalent resistivity which turned out to be a linear function of current concentration.

More[5] calculated the distributed, time dependent temperature rise and resistance of the rails as follows.

The current density j in the rails is given by

$$j = \frac{\partial H}{\partial y} \quad , \tag{A-1}$$

where H is the magnetic field, and y is the semi-infinite dimension normal to the rail surface. Because the dimensions of the rails are large compared to the current penetration depth, one-dimensional analysis is adequate.

The diffusion of H into the conductor is given by

$$\mu \frac{\partial H}{\partial t} = \frac{\partial}{\partial y}\left(\rho \frac{\partial H}{\partial y}\right) \quad , \tag{A-2}$$

and

$$D C_v \frac{\partial T}{\partial t} = \frac{\partial}{\partial y}\left(k \frac{\partial T}{\partial y}\right) + \rho \left(\frac{\partial H}{\partial y}\right)^2 \quad , \tag{A-3}$$

where μ is the permeability, ρ is the resistivity, C_v is the specific heat, k is the thermal conductivity, T is the temperature, D is the mass density of the rail material, and t is the time.

The electrical resistivity is assumed to be described by

$$\rho = \rho_0 + \alpha T \quad , \tag{A-4}$$

where ρ_0 is the initial resistivity and α is the temperature coefficient.

(A-1) through (A-4) are solved as implicit finite-difference equations, producing the temperature profile and resistance of the rails as functions of time, rail dimensions, and total current. Figures A-1, A-2 and A-3 are typical sets of current, temperature, and resistivity profiles as functions of time, respectively.

Next, the energy En dissipated in each zone was calculated from

$$E_n = \int I_n^2 R_n \, dt \quad , \tag{A-5}$$

where In and Rn are the current and resistance of the nth zone. The total energy E_R dissipated in all the zones, was equated to the dissipation in an equivalent resistance Req, i.e.,

$$E_R = \sum E_n \equiv \int I^2 R_{eq} \, dt \quad , \tag{A-6}$$

where I is the total current. The equivalent resistance was then used to find an equivalent resistivity ρ_{eq}. The equivalent resistivity of several current concentrations (current per unit rail width) were calculated in this manner. It was found that the equivalent resistivity ρ_{eq} varied linearly with the current concentration, leading to the simple relation

$$\rho_{eq} = \rho_0 + \beta \left(\frac{I}{p}\right) \quad , \tag{A-7}$$

where ρ_0 is the initial resistivity, β is the current concentration dependent component of resistivity, and p is the rail width (see Fig. A-4). The form of (A-7) was used to calculate the effective resistivity of the MFCG (8) and the railgun (1) conductors.
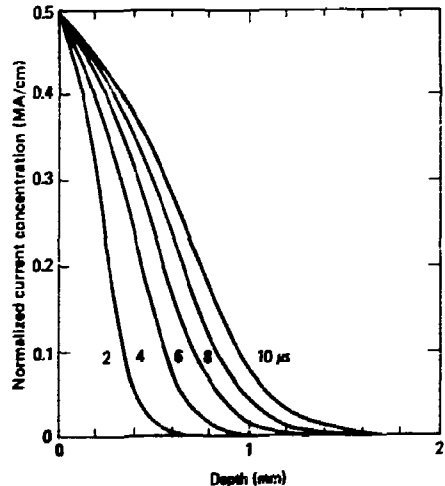
Fig. A-1. Normalized current diffusion vs depth in copper for a current concentration of 0.5 MA/cm.
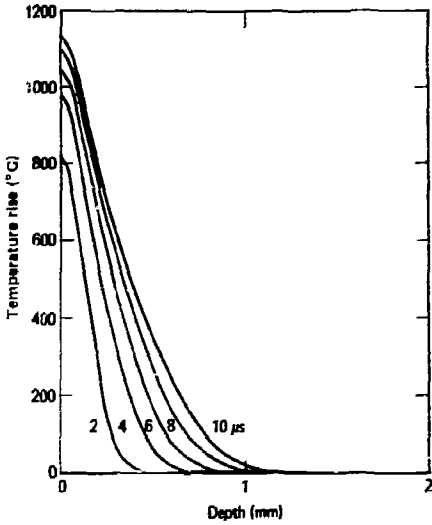
Fig. A-2. Temperature vs depth in copper for a
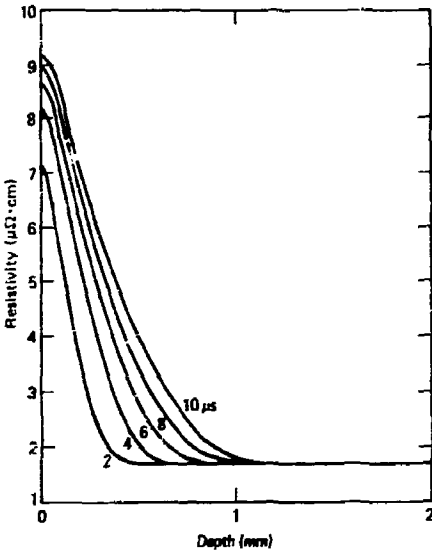current concentration of 0.5 MA/cm.

Fig. A-3. Resistivity vs depth in copper for a
current concentration of 0.5 MA/cm.
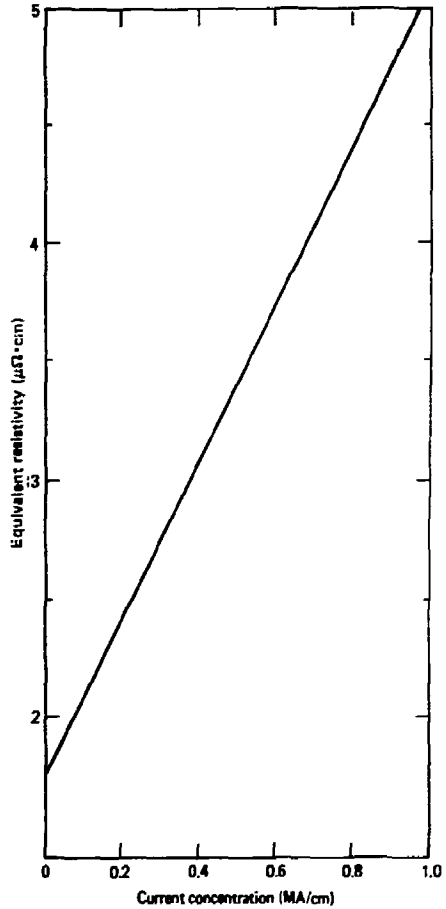
Fig. A-4. Equivalent resistivity of copper vs
current concentration.

APPENDIX B.   DERIVATION OF RESISTANCE OF
MFCG AND RAILGUN CONDUCTORS

MFCG

The current diffuses into the MFCG conductors
uniformly along its length. The effective resistance
R per unit length 1 of each of the MFCG conductors
is given by

$$\frac{R}{1} \equiv R_{1F} = \frac{\rho_F}{p_F \delta} \ , \tag{B-1}$$

where R_{1F} is the MFCG resistance gradient, ρ_F is
the resistivity of the MFCG conductors, p_F is the
width of the conductors, and δ is the skin depth of
the diffused current at time t.

9

$$\delta = \left(\frac{2\rho_p t}{\eta \mu}\right)^{1/2} \quad . \tag{B-2}$$

where μ is the permeability of the conductors. Combining (B-1) and (B-2) we have,

$$R_{1F} = \frac{\rho_F}{\rho_F \left(\frac{2\rho_F t}{\eta \mu}\right)^{1/2}} = \frac{1}{\rho_F}\left(\frac{\eta \mu \rho_F}{2t}\right)^{1/2} \quad . \tag{B-3}$$

Railgun

Unlike the MFCG, the time that the current has had to diffuse into the rails is not uniform, but is a function of the time at each point along the rails that has passed since the projectile armature has passed that point (see Fig. B-1). Assume the total current I behind the projectile is constant, then the position X of the armature (assumed to have zero thickness) is given by

$$X = \frac{1}{2}\iint a \, dt^2 = \frac{1}{2}a t^2 \quad , \tag{B-4}$$

where a and m are the acceleration and mass of the projectile, respectively. The skin depth, $\delta(x)$, at point x, along each rail is given by

$$\delta(x) = \left(\frac{2\rho \Delta t(x)}{\rho \mu}\right)^{1/2} \quad , \tag{B-5}$$

where Δt is the time since the time $t(x)$ of the passage of the armature at point x.

From Eq. (B-4),

$$x = \frac{1}{2}a t(x)^2 \quad , \tag{B-6}$$

we have

$$\Delta t = t - t(x) = \left(\frac{2}{a}\right)^{1/2}\left(X^{1/2} - x^{1/2}\right) \quad . \tag{B-7}$$

Hence,

$$\delta(x) = \left[\frac{2\rho}{\eta \mu}\left(\frac{2}{a}\right)^{1/2}\left(X^{1/2} - x^{1/2}\right)^{1/2}\right] \quad . \tag{B-8}$$

A short element dx of resistance R(x) at the point x is

$$R(x) = \frac{\rho dx}{p \delta(x)} \quad , \tag{B-9}$$

where p is the width of the rails. The total resistance R of each rail is then

$$R = \int_0^X R(x) \, dx = \int_0^X \frac{\rho dx}{p \delta(x)} \quad . \tag{B-10}$$

Substituting (B-8) into (B-10) we get

$$R = \int_0^X \frac{\rho dx}{p\left[\frac{2\rho}{\eta \mu}\left(\frac{2}{a}\right)^{1/2}\left(X^{1/2} - x^{1/2}\right)\right]^{1/2}} \tag{B-11}$$

$$= \frac{1}{p}\left(\frac{\eta \mu}{2}\right)^{1/2}\left(\frac{a}{2}\right)^{1/4}\left(\frac{8}{3}X^{3/4}\right) \quad . \tag{B-12}$$

The average resistance gradient R_1 is

$$R_1 \equiv \frac{R}{X} = \frac{8}{3p}\left(\frac{\eta \mu}{2}\right)^{1/2}\left(\frac{a}{2}\right)^{1/4}X^{-1/4} \tag{B-13}$$
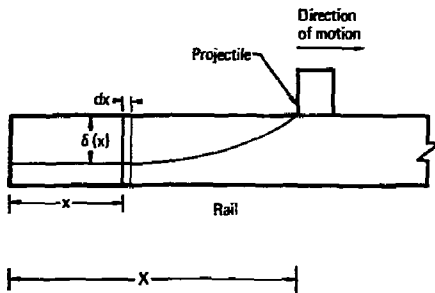

Fig. B-1. Representation of current diffusion into a rail behind an accelerating projectile. The current diffusion is shown in terms of the equivalent skin depth.

$$= \frac{8}{3p}\left(\frac{\eta \mu \rho}{2t}\right)^{1/2} \quad . \tag{B-14}$$

(Note that (B-14) compared to the uniform diffusion case of (B-3) indicates a resistance increase by a factor of 8/3.)

The preceding result is for constant current resulting in constant acceleration. In the case of nonconstant current, the rate of change of current is usually slow resembling a quasi-constant current. Furthermore, the majority of the resistance is in the region close behind the projectile because the current has had less time to diffuse into the rails in that region. This further lessens the effect of time variation of current on the resistance. Hence, (B-14) is a reasonable approximation of the resistance for most of the railguns we have modeled.

APPENDIX C. TIME-DEPENDENT MFCG INDUCTANCE GRADIENT

The intense currents in the MFCG railgun system generate intense magnetic fields which together exert strong forces on all the current carriers (the same forces that accelerate the projectile). These forces drive the inertially but not rigidly confined MFCG conductors apart. The increased spacing of the conductors leads to an increase in inductance gradient which influences the overall system operation.

The force F per unit length z driving the MFCG conductors apart is [6]

$$\frac{F}{z} = \frac{\mu_0}{2\pi}\left(\frac{I}{p_F}\right)^2\left[2 p_F \tan^{-1}\left(\frac{p_F}{w_F}\right) - w_F \ln\left(\frac{w_F^2 + p_F^2}{w_F^2}\right)\right] , \tag{C-1}$$

where w_F and p_F are the separation and width of the MFCG conductors. The inductance gradient L_{1F} of the MFCG conductor pair can be approximated by

$$L_{1F} \cong L/z = 0.794\left[\tan^{-1}\left(w_F/p_F\right)1.021\right] \quad . \tag{C-2}$$

The form of (C-1) is taken from Ref. [7] and normalized to the measured inductance of the MFCG. It is a close fit for w_F/p_F ratios from its initial value of 1 to more than its expanded value of about 2.

The complete time- and current-dependent performance of the MFCG is modeled with (C-1) and (C-2) and the appropriate derivatives.

REFERENCES

[1] C. M. Fowler, D. R. Peterson, R. S. Caird, and D. J. Erickson, B. L. Freeman, and J. C. King, "Explosive Flux Compression Generators as Railgun Power Sources," presented at the Conference on Electromagnetic Guns and Launchers, Nov. 4-6, 1980, San Diego, CA. Published as Los Alamos National Laboratory, Los Alamos, NM, Report LA-UR-80-2542 (1980).

[2] R. S. Hawke and J. K. Scudder, "Magnetic Propulsion Railguns: Their Design and Capabilities," presented at the Second International Conference on Megagauss Magnetic Field Generation and Related Topics, May 29-June 1, 1979, Washington, D.C., (to be published). Also published as Lawrence Livermore National Laboratory, Livermore, CA, Report UCRL-82677 (1979).

[3] S. C. Rashleigh and R. A. Marshall, J. Appl. Phys. 49, 2540 (1978).

[4] R. S. Hawke, A. L. Brooks, F. J. Deadrick, J. K. Scudder, C. M. Fowler, R. S. Caird, and D. R. Peterson, "Results of Railgun Experiments Powered by Magnetic Flux Compression Generators," presented at the Conference on Electromagnetic Guns and Launchers, Nov. 4-6, 1980, San Diego, CA. Published as Lawrence Livermore National Laboratory, Livermore, CA, Report UCRL-84875 (1980).

[5] R. Hoxe, Lawrence Livermore National Laboratory, Livermore, CA, private communication (1979).

[6] S. Seely, Introduction to Electromagnetic Fields (McGraw-Hill, Inc., New York, 1958).

[7] H. Knoepfel, Pulsed High Magnetic Fields (North-Holland Publishing Co., Amsterdam, 1970).

Biography

Frederick J. Deadrick was born in Paynesville,
Minnesota, on January 26, 1939. He received the BEE
degree in electrical engineering from the University of
Minnesota in 1962 and the MS degree in electrical
engineering and computer science from the University of
California, Davis, in 1972.

Since joining the Lawrence Livermore National
Laboratory in 1962, he has been active in the use of
time-domain measurement techniques in electromagnetics and
EM computer modeling and simulations. Recent work has
been in railgun modeling and testing.